ARTICLES

Journal of Semiconductors
(2023) 44, 102101
doi: 10.1088/1674-4926/44/10/102101

Pressure-dependent electronic, optical, and mechanical properties of antiperovskite X_3NP (X = Ca, Mg): A first-principles study

Chunbao Feng[1, 2], Changhe Wu[1], Xin Luo[1], Tao Hu[1], Fanchuan Chen[1], Shichang Li[1, 2], Shengnan Duan[1, 2], Wenjie Hou[3], Dengfeng Li[1, 2, †], Gang Tang[4, †], and Gang Zhang[5, †]

[1]School of Science, Chongqing University of Posts and Telecommunications, Chongqing 400065, China

[2]Institute for Advanced Sciences, Chongqing University of Posts and Telecommunications, Chongqing 400065, China

[3]School of Computer Science and Technology, Northwestern Polytechnical University, Xi'an 710129, China

[4]Advanced Research Institute of Multidisciplinary Science, Beijing Institute of Technology, Beijing 100081, China

[5]Institute of High Performance Computing, A*STAR, 138632, Singapore

Abstract: Hydrostatic pressure provides an efficient way to tune and optimize the properties of solid materials without changing their composition. In this work, we investigate the electronic, optical, and mechanical properties of antiperovskite X_3NP (X^{2+} = Ca, Mg) upon compression by first-principles calculations. Our results reveal that the system is anisotropic, and the lattice constant *a* of X_3NP exhibits the fastest rate of decrease upon compression among the three directions, which is different from the typical *Pnma* phase of halide and chalcogenide perovskites. Meanwhile, Ca_3NP has higher compressibility than Mg_3NP due to its small bulk modulus. The electronic and optical properties of Mg_3NP show small fluctuations upon compression, but those of Ca_3NP are more sensitive to pressure due to its higher compressibility and lower unoccupied 3*d* orbital energy. For example, the band gap, lattice dielectric constant, and exciton binding energy of Ca_3NP decrease rapidly as the pressure increases. In addition, the increase in pressure significantly improves the optical absorption and theoretical conversion efficiency of Ca_3NP. Finally, the mechanical properties of X_3NP are also increased upon compression due to the reduction in bond length, while inducing a brittle-to-ductile transition. Our research provides theoretical guidance and insights for future experimental tuning of the physical properties of antiperovskite semiconductors by pressure.

Key words: antiperovskite; hydrostatic pressure; physical properties; first-principles calculations

Citation: C B Feng, C H Wu, X Luo, T Hu, F C Chen, S C Li, S N Duan, W J Hou, D F Li, G Tang, and G Zhang, Pressure-dependent electronic, optical, and mechanical properties of antiperovskite X_3NP (X = Ca, Mg): A first-principles study[J]. *J. Semicond.*, 2023, 44(10), 102101. https://doi.org/10.1088/1674-4926/44/10/102101

1. Introduction

Lead-based halide perovskite solar cell materials have received much attention because of their excellent properties such as suitable direct band gap, high optical absorption, long diffusion length, and long carrier lifetime[1–5]. Since halide perovskites were reported in 2009, they have sparked research interest, with solar cell power conversion efficiency (PCE) increasing at an impressive rate from 3.8% to the current 25.7%[6, 7]. Despite the excellent photovoltaic properties and the rapid development of lead halide perovskites, there are two unavoidable challenges. The first challenge is that lead halide perovskites are highly susceptible to degradation when encountering water or air, leading to instability. The other challenge is the toxicity of lead[8–10]. In particular, the search for lead-free optoelectronic semiconductors that can match the performance of lead-based halide perovskites is very challenging.

Recently, Tang et al. and coauthors proposed an ion-type inversion strategy to design a new class of antiperovskite semiconductors with optoelectronic properties similar to those of lead-based halide perovskites[11, 12]. Antiperovskite X_3BA (X is a cation, A and B are different-sized anions) has the same perovskite-type crystal structure as the conventional perovskite ABX_3 (A and B are different-sized cations, X is an anion), but the positions of the anions and cations at the lattice sites are swapped. Among them, nitride antiperovskites X_3NA with the anion N^{3-} located in the center of the octahedron have attracted extensive research interest due to the unique features of the nitrogen element[13–15]. So far, at least 16 experimental syntheses of X_3NA (X_3NE (X = Sr, Ba; E = Sb, Bi)[16, 17]; Mg_3NPn (Pn = As, Sb)[18]; Ca_3NM (M = P, As, Sb, Bi, Ge, Sn, Pb, Tl)[19, 20]; and A_3NAs (A = Mg, Ca, Sr, Ba)[21]) have been reported. The physical properties of X_3NA have been widely studied, including optoelectronic[22, 23], superconductivity[24–27], magnetoresistance[28, 29], magnetostriction[30], magnetic and magnetocaloric[31], thermoelectricity[32, 33], negative thermal expansion[34, 35], Dirac semi-metallic characteristic[36, 37], and topological insulators characteristic[38]. Among nitride antiperovskites X_3NA (X = Sr^{2+}, Ca^{2+}, Mg^{2+}; A = P^{3-}, Sb^{3-}, Bi^{3-}), Sr_3PN have suitable band gaps ~1.2 eV, but others have band gaps that are too large for solar cell applications[13–15, 39]. For example, Ca_3NP and Mg_3NP have wide direct band gaps of 2.1 eV and 2.3 eV, respectively[39]. In addi-

Correspondence to: D F Li, lidf@cqupt.edu.cn; G Tang, gtang@bit.edu.cn; G Zhang, zhangg@ihpc.a-star.edu.sg
Received 18 APRIL 2023.
©2023 Chinese Institute of Electronics

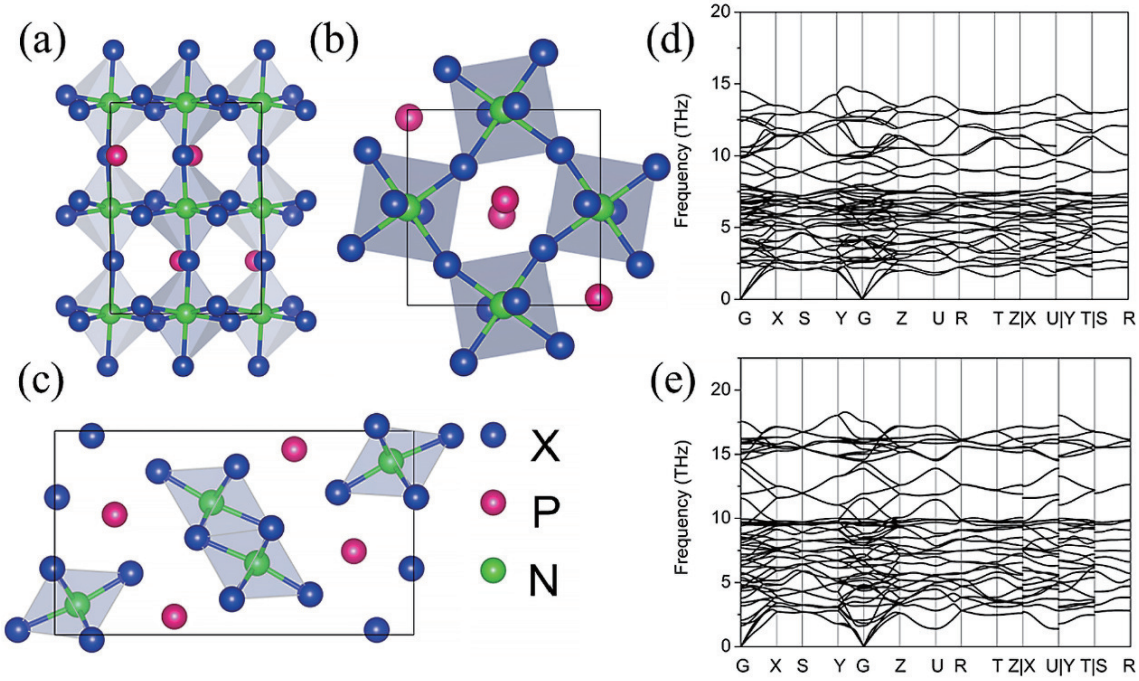

Fig. 1. (Color online) (a) Side view and (b) top view of the atomic structure of *Pnma* (3D). (c) Top view of the atomic structure of *Pnma* (1D). Phonon spectra for (d) Ca_3NP and (e) Mg_3NP with *Pnma* (3D) space group. Visualization was performed with VESTA[50].

tion to compositional engineering, strain and pressure are also important ways to modulate the electronic and optical properties of materials by tuning interatomic distance without changing the material composition. At present, a variety of pressure-induced phenomena have been found in perovskites, such as structural phase transition [40–42], semiconductor-to-metal transition[43, 44], bandgap optimization[44–47], emergence of photoluminescence[40, 48], crystalline to amorphous transitions[49], and so on. However, the effect of pressure on the physical properties of antiperovskite materials has been relatively unexplored, except for a few studies reporting pressure-induced structural phase transitions (e.g., Ni_3CMg)[41] and semiconductor-to-metal transition (e.g., Ca_3NP)[44]. In particular, studies exploring the structure-property relationships of antiperovskite compounds under pressure are rare.

In this work, taking two large-bandgap antiperovskites X_3NP (X^{2+} = Ca, Mg) as examples, we studied the effect of pressure on their electronic, optical, and mechanical properties using first-principles calculations. We first investigated the structural stability and equation of state of X_3NP under pressure. We then calculated the trend of the optoelectronic properties of X_3NP with the pressure. The results reveal that the electronic (i.e., band gap, carrier effective masses), dielectronic, exciton binding energy, and optical properties of Mg_3NP show relatively small fluctuations upon compression, but those of Ca_3NP are more sensitive to pressure. The different pressure-dependent optoelectronic properties in Mg_3NP and Ca_3NP were analyzed in detail. Finally, the mechanical properties of X_3NP under compression were investigated.

2. Results and discussions

2.1. Crystal structure, equation of state, and dynamics stability under pressure

From previous studies[44], it was found that the main competing phases of X_3NP (X = Ca, Mg) are one-dimensional (1D) and three-dimensional (3D) *Pnma* phases at pressure below 40 GPa, as shown in Figs. 1(a) and 1(c). It can be seen that the 3D *Pnma* phase consists of highly distorted $[NX_6]$ octahedra that are connected by means of corner-sharing, while the 1D *Pnma* phase shows edge-sharing octahedra. The calculated total energy and phonon spectra confirm the thermal and dynamic stability of the 3D *Pnma* phase of X_3NP (X = Ca, Mg), as shown in Figs. 1(d) and 1(e).

Considering whether the increase in pressure leads to a phase transition in X_3NP (X = Ca, Mg), we calculated the total enthalpy ($H = E + PV$) differences ($\Delta H = H_{tot}(1D) - H_{tot}(3D)$) of *Pnma* between 1D and 3D. From 0 to 20 GPa, ΔH is greater than 0 for Ca_3NP and Mg_3NP up to 40 GPa. Moreover, the phonon spectra of the two compounds from 0 to 20 GPa (see Figs. 1(d) and 1(e), and Fig. S3) do not exhibit any imaginary phonon modes, indicating that they are all thermally and dynamically stable in the 3D phase throughout this pressure range.

As shown in Fig. 2, the lattice constants and volumes of X_3NP (X^{2+} = Ca, Mg) decrease linearly with increasing pressure from 0 to 20 GPa. Specifically, Ca_3NP (Mg_3NP) shortens by 7.4% (5.2%), 5.9% (4.5%), and 6.1% (4.9%) in the *a*, *b*, and *c* directions, respectively, as shown in Table S1. The volume reduction of 18.3% (13.9%) indicates that Ca_3NP is more compressive than Mg_3NP. The compression in X_3NP (X = Ca, Mg) shows a rate of decline $a > b > c$ direction, as shown in Figs. 2(a) and 2(c), implying compressibility $a > b > c$ axis. It is obvious that the trend of lattice parameters with pressure is contrary to that of conventional halide perovskites and chalcogenide perovskites[51, 52]. For example, for the same orthorhombic phase *Pnma*, the highest compressibility is along the *b*-axis in inorganic halide perovskites and along the *c*-axis in chalcogenide perovskites. The equations of state (EOS) of both Ca_3NP and Mg_3NP are presented in Figs. 2(b) and 2(d), respectively. The pressure versus volume curves were fitted compressive using a third-order Birch-Murnaghan EOS fit. It is worth mentioning that the bulk modulus and the elastic con-

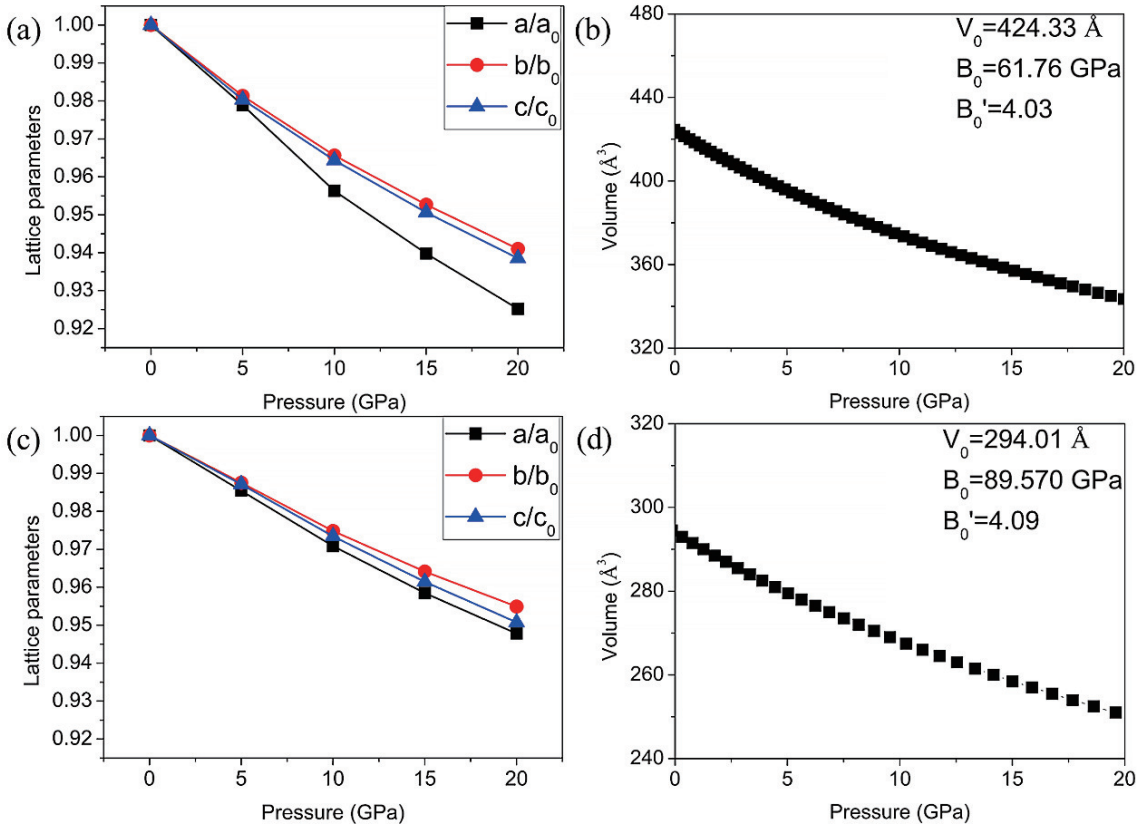

Fig. 2. (Color online) (a) Evolution of lattice parameters with pressure and (b) equation of state of Ca_3NP. (c) Evolution of lattice parameters with pressure and (d) equation of state of Mg_3NP.

stants in three directions of Ca_3NP are lower than those of Mg_3NP, the ambient pressure bulk moduli of Ca_3NP and Mg_3NP are 61.76 and 89.57 GPa, respectively, as shown in Figs. 2(b) and 2(d), which make the compressibility of Ca_3NP higher than that of Mg_3NP. These results are close to the values reported in Table S5.

2.2. Evolution of electronic properties under pressure

The band structures and partial density of states (PDOS) of X_3NP (X = Ca, Mg) at different pressures based on the HSE06 method are shown in Figs. S5 and S6. First, it can be seen that X_3NP (X = Ca, Mg) maintains a direct band gap at Γ-point from 0 to 20 GPa. Second, the band gap of X_3NP (X = Ca, Mg) almost linearly decreases with increasing pressure, as shown in Table S4 and Fig. 3(a). Specifically, the band gap of Ca_3NP decreases with increasing pressure from 2.136 eV at 0 GPa to 1.767 eV at 20 GPa, a decrease of 17.3%. In contrast, Mg_3NP decreases only 2.79% from 2.366 eV at 0 GPa to 2.300 eV at 20 GPa. In the following, we will analyze in detail the reasons for the apparently different pressure-dependent bandgap variations of Ca_3NP and Mg_3NP.

The PDOS of Ca_3NP shows that the conduction band minimum (CBM) is mainly contributed by the cation Ca *d* orbital, and anion and cation *s* orbitals, while the valence band maximum (VBM) consists mainly of the *p* orbitals of P and N, as shown in Figs. S5(c) and S5(d). As the pressure increases, CBM of Ca_3NP shift down, leading to a significant decrease in the band gap, as shown in Figs. S5(a) and S5(b) and Figs. S7(a) and S7(d). In Mg_3NP, the CBM is contributed mostly by the cation and anion *s* orbitals and the VBM is mainly contributed by the *p* orbitals of P/N, as shown in Figs. S6(c) and S6(d). Unlike Ca_3NP, the CBM and VBM of Mg_3NP move only slightly with increasing pressure, and the upward shift of VBM is more pronounced, which causes a slight decrease in the band gap, as shown in Figs. S6(a) and S6(b) and Figs. S7(e)–S7(h). According to PDOS in Fig S5 and Fig S6, VBM is a P+N *p* state and CBM is a cation+anion *s* and cation *d* state, under pressure, CBM drops in energy due to *s-d* repulsion, which is large for Ca than for Mg because Ca 3*d* orbital energy is closer to the conduction band edge, so the Ca band gap drops faster than Mg. The VBM drops due to *p-p* repulsion between cation and anions but is also pushed up due to *p-p* repulsion between P and N, so its change is relatively small. Therefore, compared to Ca_3NP, the small band gap reduction of Mg_3NP with increasing pressure could be attributed to the low *d* orbital contribution and the low lattice constant compressibility.

Carrier effective mass (m^*) is another important descriptor that can be used to assess the electronic properties of photovoltaic materials. The hole and electron effective masses of X_3NP (X= Ca, Mg) under different pressure are shown in Fig. 3(b) and Table S3. It can be seen that the average hole m_h (electron m_e) effective masses of Ca_3NP and Mg_3NP are 0.636 (0.530) and 0.568 (0.336) m_0 at 0 GPa, respectively. Compared to the *p-d* orbital hybridization in Ca_3NP, the CBM and VBM of Mg_3NP are contributed by *s-p* and *p-p* orbital hybridization[53]. Therefore, Mg_3NP has relatively dispersed bands near the Fermi level and small carrier effective masses. As the pressure increases, the average m_e of Mg_3NP and Ca_3NP show small fluctuations, and the average m_h of Ca_3NP shows a monotonic decreasing trend, while the average m_h of Mg_3NP has small variation. A gradual decrease in the m_h of Ca_3NP is attributed to the increase in the P and N *p-p* repulsion and increased bandwidth of the valence band by the pressure, as

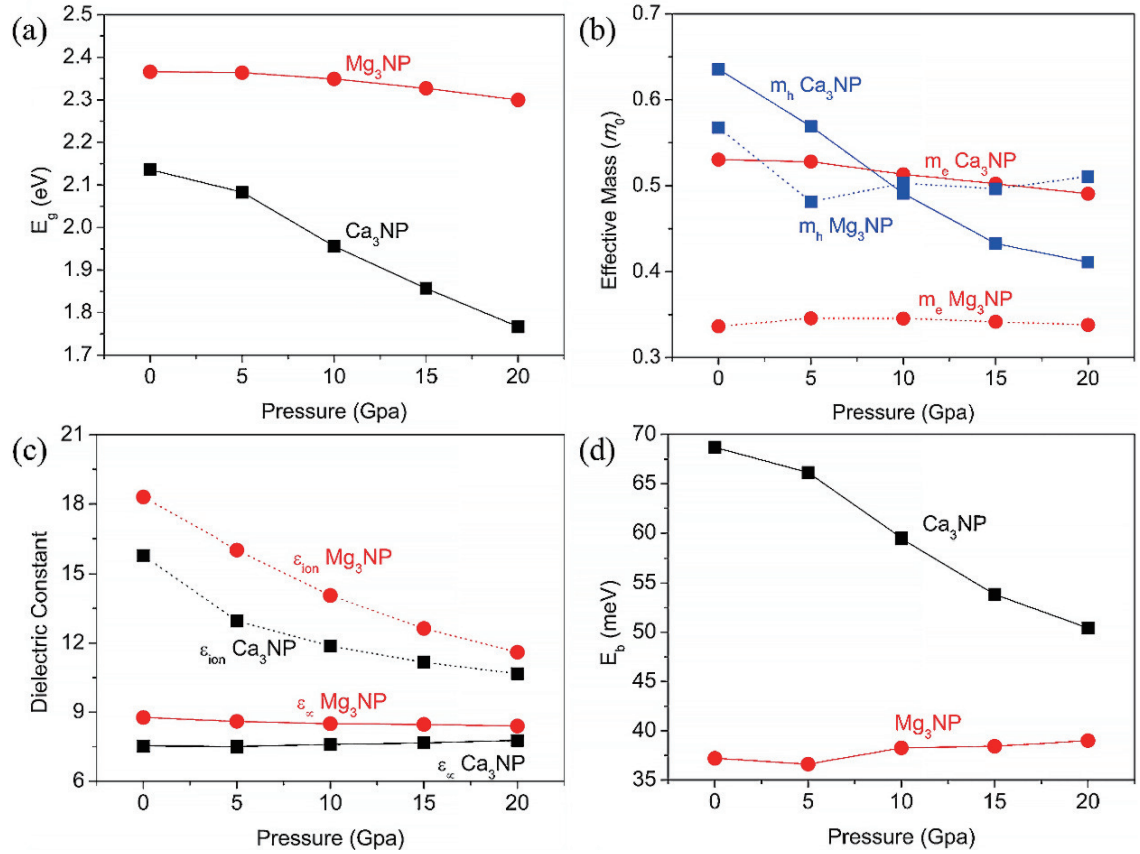

Fig. 3. (Color online) (a) The bandgap of Ca_3NP (square) and Mg_3NP (circle), (b) the average hole (square) and electronic (circle) effective masses (m_0) of Ca_3NP (line) and Mg_3NP (dot), (c) the electronic (line) and ionic (dot) dielectric constant of Ca_3NP (square) and Mg_3NP (circle), and (d) the exciton binding energy (meV) of Ca_3NP (square) and Mg_3NP (circle) under different pressures.

seen in Table S4.

Static dielectric constants can also be used to evaluate carrier transport properties because they can effectively limit defects and impurities scattering[54, 55]. The static permittivity (ε_{st}) is contributed by ions (ε_{ion}) and electrons (ε_{∞}), where the electronic permittivity has a strong correlation with the electronic properties[11]. The dielectric constants of X_3NP (X = Ca, Mg) at 0 GPa show strong anisotropy (e.g., for Ca_3NP, ε_{st}^{xx} = 23.8, ε_{st}^{yy} = 24.0, ε_{st}^{zz} = 22.3; for Mg_3NP, ε_{st}^{xx} = 29.7, ε_{st}^{yy} = 27.7, ε_{st}^{zz} = 23.6), as shown in Table S6, which are higher than that of typical halide perovskite $CsPbBr_3$ (ε_{ion} = 14.6, ε_{∞} = 4.6, ε_{std} = 19.2)[11, 56]. The ε_{∞} of X_3NP (X = Ca, Mg) increases slightly with increasing pressure, which is caused by the reduced band gap[57], as shown in Table S4 and Fig. 3(c). However, the ε_{ion} of X_3NP (X = Ca, Mg) decreases gradually with increasing pressure, which is due to the reduced N-X bond length and increased frequency of lowest-lying optical phonon modes[58]. That is, the reduced ε_{ion} is due to increased confinement of the N ions under pressure, which limits the ion movement.

The exciton binding energy E_b of X_3NP (X = Ca, Mg) is obtained based on the calculated effective mass and electronic dielectric constant. The small exciton binding energy is an essential basis for determining the ideal solar cell material because the smaller exciton binding energy (E_b) enables the rapid separation of photogenerated carriers[59]. The E_b is calculated using the Wannier model[60]:

$$E_b = R_y \frac{\mu^*}{\varepsilon^2}, \quad (1)$$

where R_y = 13.56 eV is the atomic Rydberg energy, μ^* is the reduced exciton mass ($1/\mu^* = 1/m_e + 1/m_h$), and ε is the electronic dielectric constant. It can be seen that the E_b of Ca_3NP and Mg_3NP are 69 and 37 meV at 0 GPa, respectively. As the pressure increases, the E_b of Ca_3NP shows a monotonic decreasing trend and Mg_3NP shows small fluctuations, as shown in Table S4 and Fig. 3(d). The large decrease of the exciton binding energy of Ca compound is due to the increased Ca *d* component in CBM whereas the VBM is anion *p* state. The slight increase of the exciton binding energy of the Mg compound is due to the volume confinement.

2.3. Optical absorption and power conversion efficiency under pressure

The optical absorption in the visible region is key for optoelectronic application. The optical absorption of X_3NP (X = Ca, Mg) is anisotropic along different directions at different pressures, as shown in Fig. S8. The optical absorption coefficients ($\alpha \sim 10^5$ cm^{-1}) of X_3NP (X = Ca, Mg) in the visible region (see Fig. 4(a)) are comparable to the experimentally derived $CH_3NH_3PbI_3$[61]. In the range of pressure from 0 to 20 GPa, Ca_3NP has a more pronounced redshift than Mg_3NP and an overall higher absorption coefficient in the visible region, as shown in Fig. 4(a). This corresponds exactly to the magnitude and size of their band gap variation, with the suitable band gap being more efficient in optical absorption.

The spectroscopic limited maximum efficiency (SLME) method is very effective in evaluating PV performance in terms of band gap and optical absorption strength, and identifying and analyzing promising PV materials[62, 63]. The maxi-

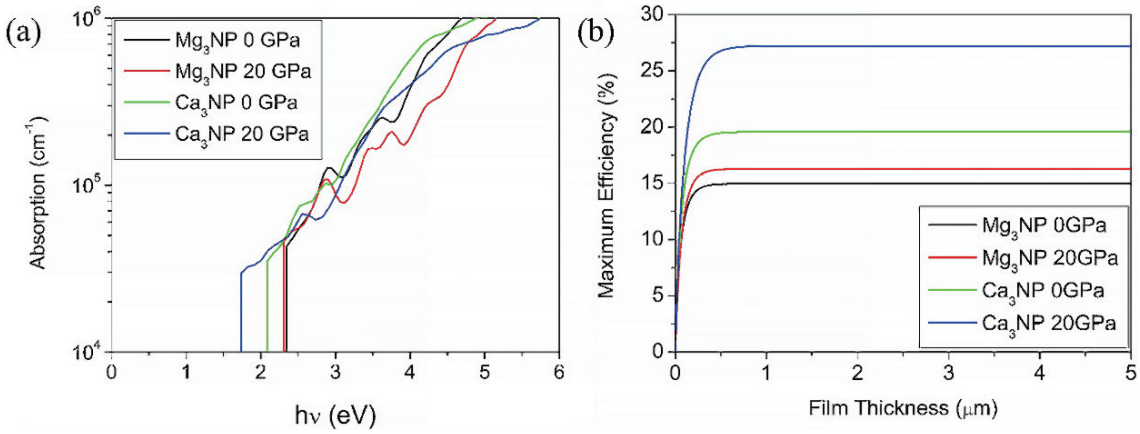

Fig. 4. (Color online) (a) The optical absorption and (b) SLME of Ca_3NP and Mg_3NP under different pressures.

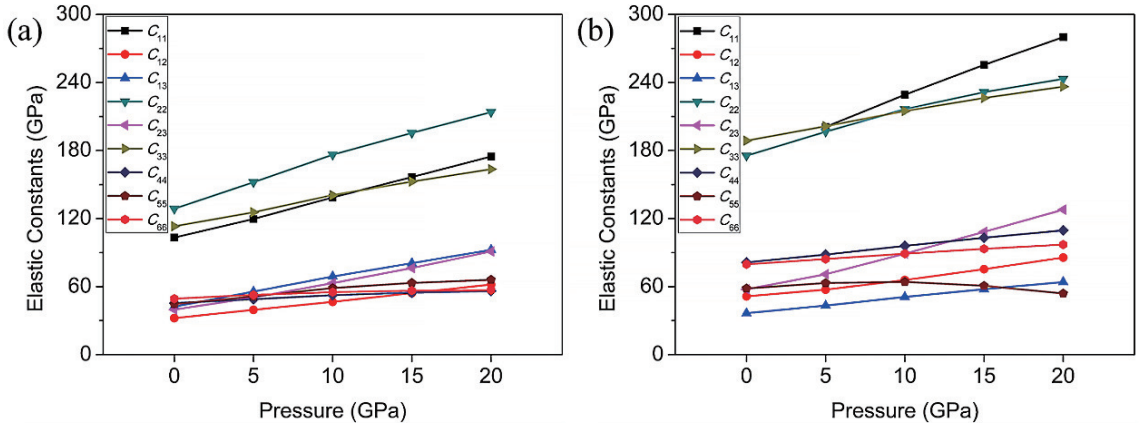

Fig. 5. (Color online) The elastic constants of (a) Ca_3NP and (b) Mg_3NP under different pressures.

mum conversion efficiency is closely related to the thickness of the film, as shown in Fig. 4(b). We show that the maximum SLME of 19.629% (15%) and 27.5% (16%) can be reached at 0 and 20 GPa for Ca_3NP (Mg_3NP) with a film thickness of 0.5 μm, respectively. The optical absorption of Mg_3NP is changed only slightly, which makes the SLME only increase by 1%. When Ca_3NP is at 20 GPa, SLME is comparable to conventional lead-based halide perovskites $MAPbI_3$ (~30.90%)[12] and $CsPbI_3$ (~29.4%)[64]. At 20 GPa, the smaller band gap and the redshift of the optical absorption coefficient are the main mechanisms for the increase in theoretical efficiency; that is, improved SLME is due to increase absorption (current) due to the reduced band gap.

2.4. Mechanical properties under pressure

The mechanical properties of a material have a very large impact on the actual solar cell preparation[65, 66]. We examine the mechanical stability of X_3NP (X = Ca, Mg) under different pressure by calculating the elastic constants (C_{ij}). For orthorhombic structure (SG *Pnma*) with nine independent elastic constants and X_3NP (X = Ca, Mg) satisfying mechanical stability. The values of the elastic constants for both at different pressure are shown in Table S5, and the mechanical stability criteria for SG *Pnma* are shown in the Supplemental Material, Sec. Ⅲ. The elastic constants of both have significant elastic anisotropy. The principal elastic constants of X_3NP (X = Ca, Mg) are C_{11}, C_{22}, and C_{33}, and they reflect the strong resistance of the crystal to deformation along the *a*-, *b*- and *c*-directions, respectively. The C_{11}, C_{22}, and C_{33} of Ca_3NP (Mg_3NP) were 103.3 (176.1), 128.7 (175.4), and 113.2 (188.7) GPa, respectively. Here, in terms of uniaxial strain, the Ca_3NP and Mg_3NP crystals have the highest compressibility along the *b*- and *c*-axes, respectively, while the lowest compressibility is along the *c*- and *b*-axes, respectively, as shown in Table S5. Furthermore, the elastic constants of Ca_3NP (Mg_3NP) satisfy C_{44} = 45.5 GPa (81.4 GPa) < (C_{11}, C_{22}, C_{33}), which means that both are susceptible to shear deformation[67]. The elastic constant of X_3NP (X = Ca, Mg) has a tendency to increase in the pressure range from 0 to 20 GPa, except for a decrease of 4.45 GPa for the elastic constant C_{55} of Mg_3NP. Ca_3NP and Mg_3NP are driven by the pressure with a rapid linear increase of C_{22} and C_{11}, respectively, and their values exceed the other elastic constants, as shown in Fig. 5. The chalcogenide perovskite $AZrS_3$ (A = Mg, Ca, Sr and Ba) reported by Majumdar[52] and Rong[68] *et al.*, also has an orthorhombic structure where the elastic constants increase with decreasing lattice constants. Therefore, the increase in the elastic constants should be caused by the shortening of the lattice constants and bond lengths due to the increase in pressure. The increased elastic constant is due to short bond length or increased covalency.

Meanwhile Young's modulus (*Y*), bulk modulus (*B*), shear modulus (*G*) and Poisson's ratio (υ) are calculated by Voigt-Reuss-Hill (VRH)[69, 70] approximation based on the corresponding elastic constants, as summed in Table S5, specific relationships in Supplemental Material, Sec. III. *Y*, *B*, and *G* represent the material's resistance to against longitudinal tension, resistance to fracture and resistance to plastic deformation, respec-

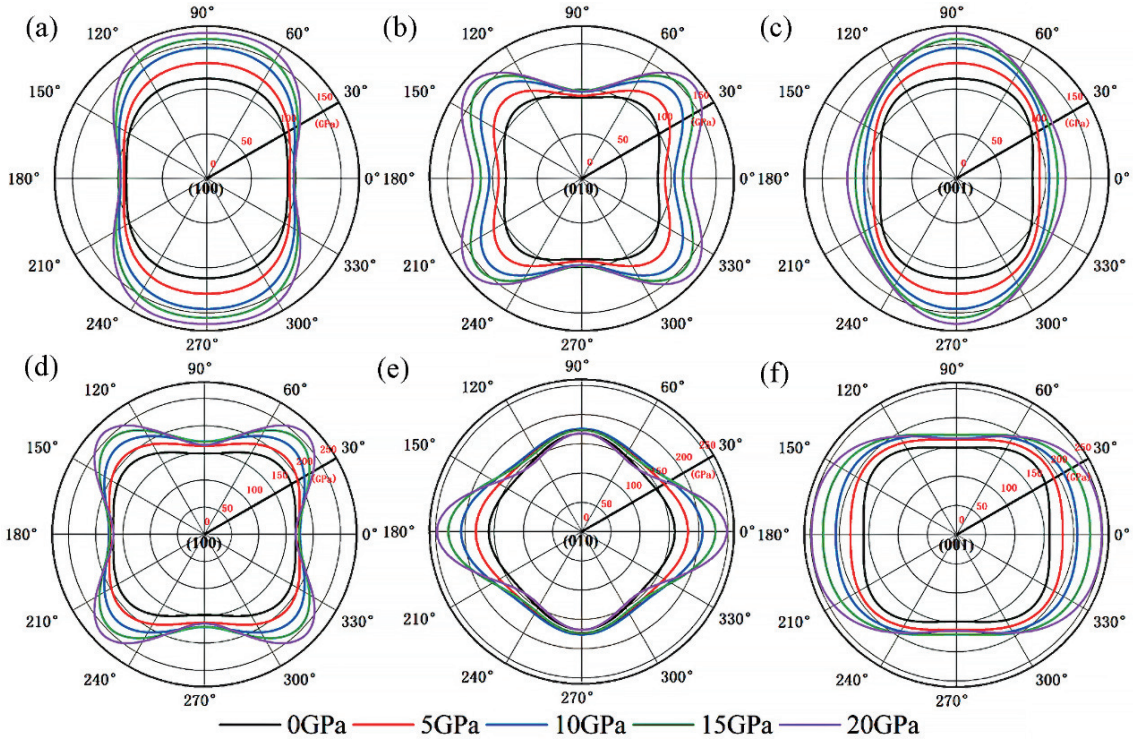

Fig. 6. (Color online) The orientational-dependence of Young's modulus *Y* (GPa) along the (a) (100), (b) (010), (c) (001) planes for Ca_3NP and the (d) (100), (e) (010), (f) (001) planes for Mg_3NP under different pressures.

tively[71]. X_3NP (X = Ca, Mg) increases with increasing pressure in the interval from 0 to 20 GPa for *Y*, *B* and *G*, and the increase in modulus is approximately the same for both. The increase in pressure causes the bond length to decrease, resulting in a progressive increase in *Y* for X_3NP (X = Ca, Mg). This happens because larger strains are usually required to break smaller bond lengths, and thus obtain elastic constants and larger Young's modulus[11]. In addition, the elastic properties of perovskites are mainly determined by the strength of the chemical bond X–B[72, 73]. As the radius of the cation at the X-site decreases [$r(Ca^{2+}) > r(Mg^{2+})$], the elastic constants and *Y* of the corresponding compounds increase with the shortening of the X-N bond length. This implies that Mg_3NP has a larger C_{ij} and *Y* compared to Ca_3NP, which is confirmed in Table S5. X_3NP (X = Ca, Mg) has the largest increase in *B*, while *G* is the least sensitive to pressure.

To better represent the orientation-dependent *Y*, we plotted the (100), (010) and (001) planar 2D projections of *Y* in polar coordinates for X_3NP (X = Ca, Mg) under different pressures, as shown in Fig. 6. The three planes of X_3NP (X = Ca, Mg) under different pressure exhibit some common features, namely, apparent anisotropy, *Y* at each angle increases with increasing pressure, anisotropy becomes more prominent with increasing pressure, obvious axial symmetry in shape and clear angular characteristics. The *Y* of some angles in the plane remains unchanged or increases by a small amount under increasing pressure, while other angles increase substantially, which leads to the enhanced anisotropy. Taking Ca_3NP (100) plane as an example, the Young's modulus is almost constant at 0° and 180°, and increases rapidly at 90° and 270° along with the strengthening of the pressure, as illustrated in Fig. 6(a). In addition, the Young's modulus distributions in the same plane of X_3NP (X = Ca, Mg) are different due to the different bond lengths of Ca–N and Mg–N.

It is worth mentioning that *B*/*G* is called Pugh's ratio. The value of *B*/*G* equal to 1.75 is used as the boundary value between ductility and brittleness[74, 75]. The *B*/*G* values of Ca_3NP and Mg_3NP showed brittleness (less than 1.75) at 0–5 GPa and 0–15 GPa and ductility (higher than 1.75) at 10–20 GPa and 20 GPa, respectively, and the *B*/*G* increased with the increase of pressure, as shown in Table S5. In addition, the Poisson's ratio (*υ*) proposed by Frantsevich's rule can also be used as an indication of toughness and brittleness, with Poisson's ratio equal to 0.26 as the critical value, greater than 0.26 for toughness and less than 0.26 for brittleness[75]. In this paper, the ductility and brittleness of X_3NP (X = Ca, Mg) under different pressures are evaluated by *B*/*G* and ν methods and the results are consistent with each other. This demonstrates that X_3NP (X = Ca, Mg) shifts from brittleness to ductility as pressure increases.

3. Conclusions

In summary, we have investigated the electronic, optical, and mechanical properties of antiperovskite X_3NP (X^{2+} = Ca, Mg) in the pressure range 0–20 GPa by first-principles calculations. Our results show that X_3NP (X = Ca, Mg) shows an anisotropic compressibility with $a > b > c$ axis, which is different from the typical *Pnma* phase in halide perovskites and chalcogenide perovskites. Meanwhile, Ca_3NP (B_0 = 61.76 GPa) has higher compressibility than Mg_3NP (B_0 = 89.57 GPa) due to its small bulk modulus B_0. The electronic and optical properties of Mg_3NP show small fluctuations upon compression, but those of Ca_3NP are more sensitive to pressure. For example, as the pressure increases from 0 to 20 GPa, the band gap of Ca_3NP decreases from 2.136 to 1.767 eV, the ionic dielectric constant is reduced by 7.4%, 5.9%, and 6.1% in the *a*, *b*, and *c* directions, respectively, the exciton binding energy decreases from 69 to 50 meV, the optical absorption is significantly red-

shifted, and the SLME sharply increases from 19.6% to 27.5%. The different pressure-dependent optoelectronic properties in Mg_3NP and Ca_3NP are mainly attributed to their different lattice compressibility and band-edge orbital hybridization. Ca_3NP has lower unoccupied 3*d* orbital energy, which leads to strong *s-d* coupling at the CBM edge. Finally, the mechanical properties of X_3NP are increased upon compression due to the reduction in bond length, while inducing a brittle-to-ductile transitions for Ca_3NP and Mg_3NP at 10 and 20 GPa, respectively. Therefore, our research provides theoretical guidance and insights for future experimental tuning of the physical properties of antiperovskite semiconductors by pressure.

Acknowledgements

C.B.F. is supported by the Science and Technology Research Program of Chongqing Municipal Education Commission (Grant No. KJQN202100626). G.T. is supported by Beijing Institute of Technology Research Fund Program for Young Scholars (Grant No. XSQD-202222008). S.D. thanks the support from the National Natural Science Foundation of China (Grant No. 12204081), the Natural Science Foundation of Chongqing (Grant No. 2022NSCQ-MSX2540), the Science and Technology Research Program of Chongqing Municipal Education Commission (Grant No. KJQN202200619). The work was carried out at National Supercomputer Center in Tianjin, and this research was supported by TianHe Qingsuo Project-special fund project.

Appendix A. Supplementary material

Supplementary materials to this article can be found online at https://doi.org/1674-4926/44/10/102101.

References

[1] Brenner T M, Egger D A, Kronik L, et al. Hybrid organic-inorganic perovskites: Low-cost semiconductors with intriguing charge-transport properties. Nat Rev Mater, 2016, 1, 15007

[2] Tiwari A, Satpute N S, Mehare C M, et al. Challenges, recent advances and improvements for enhancing the efficiencies of ABX_3-based PeLEDs (perovskites light emitting diodes): A review. J Alloys Compd, 2021, 850, 156827

[3] Sun S Y, Salim T, Mathews N, et al. The origin of high efficiency in low-temperature solution-processable bilayer organometal halide hybrid solar cells. Energy Environ Sci, 2014, 7, 399

[4] Xing G C, Mathews N, Sun S Y, et al. Long-range balanced electron- and hole-transport lengths in organic-inorganic $CH_3NH_3PbI_3$. Science, 2013, 342, 344

[5] Kim J Y, Lee J W, Jung H S, et al. High-efficiency perovskite solar cells. Chem Rev, 2020, 120, 7867

[6] Kojima A, Teshima K, Shirai Y, et al. Organometal halide perovskites as visible-light sensitizers for photovoltaic cells. J Am Chem Soc, 2009, 131, 6050

[7] NREL Best Research-Cell Efficiencies. https://www.nrel.gov/pv/cell-efficiency.html (accessed March 10, 2023)

[8] Abhishek S, Marshall Ashley R, Sanehira Erin M, et al. Quantum dot-induced phase stabilization of α-$CsPbI_3$ perovskite for high-efficiency photovoltaics. Science, 2016, 354, 92

[9] Ju M G, Chen M, Zhou Y Y, et al. Toward eco-friendly and stable perovskite materials for photovoltaics. Joule, 2018, 2, 1231

[10] Fu P F, Hu S L, Tang J, et al. Material exploration via designing spatial arrangement of octahedral units: A case study of lead halide perovskites. Front Optoelectron, 2021, 14, 252

[11] Zhong H X, Feng C B, Wang H, et al. Structure–composition–property relationships in antiperovskite nitrides: Guiding a rational alloy design. ACS Appl Mater Interfaces, 2021, 13, 48516

[12] Han D, Feng C B, Du M H, et al. Design of high-performance lead-free quaternary antiperovskites for photovoltaics via ion type inversion and anion ordering. J Am Chem Soc, 2021, 143, 12369

[13] Mochizuki Y, Sung H J, Takahashi A, et al. Theoretical exploration of mixed-anion antiperovskite semiconductors M_3XN(M=Mg, Ca, Sr, Ba;X=P, As, Sb, Bi). Phys Rev Materials, 2020, 4, 044601

[14] Dai J, Ju M G, Ma L, et al. Bi(Sb)NCa_3: Expansion of perovskite photovoltaics into all-inorganic anti-perovskite materials. J Phys Chem C, 2019, 123, 6363

[15] Heinselman K N, Lany S, Perkins J D, et al. Thin film synthesis of semiconductors in the Mg–Sb–N materials system. Chem Mater, 2019, 31, 8717

[16] Gäbler F, Kirchner M, Schnelle W, et al. $(Sr_3N)E$ and $(Ba_3N)E$ (E = Sb, Bi): Synthesis, crystal structures, and physical properties. Zeitschrift Anorg Allge Chemie, 2004, 630, 2292

[17] Zada R, Ali Z, Mehmood S. Optoelectronic, elastic and thermoelectric properties of the perovskites $(Sr_3N)Sb$ and $(Sr_3N)Bi$. Mater Sci Semicond Process, 2022, 147, 106734

[18] Chi E O, Kim W S, Hur N H, et al. New Mg-based antiperovskites $PnNMg_3$ (Pn=As, Sb). Solid State Commun, 2002, 121, 309

[19] Chern M Y, Vennos D A, Disalvo F J. Synthesis, structure, and properties of anti-perovskite nitrides Ca_3MN, M=P, As, Sb, Bi, Ge, Sn, and Pb. J Solid State Chem, 1992, 96, 415

[20] Niewa R, Schnelle W, Wagner F R. Synthesis, crystal structure and physical properties of $(Ca_3N)Tl$. Z Anorg Allg Chem, 2001, 627(3), 365.

[21] Stoiber D, Niewa R. Perovskite distortion inverted: Crystal structures of $(A_3N)As$ (A = Mg, Ca, Sr, Ba). Z Anorg Allg Chem, 2019, 645, 329

[22] Iqbal S, Murtaza G, Khenata R, et al. Electronic and optical properties of Ca_3MN (M = Ge, Sn, Pb, P, As, Sb and Bi) Antiperovskite Compounds . J Electron Mater, 2016, 45, 4188

[23] Ullah I, Murtaza G, Khenata R, et al. Structural and optoelectronic properties of X_3ZN (X = Ca, Sr, Ba; Z = As, Sb, Bi) anti-perovskite compounds. J Electron Mater, 2016, 45, 3059

[24] He B, Dong C, Yang L H, et al. $CuNNi_3$: A new nitride superconductor with antiperovskite structure. Supercond Sci Technol, 2013, 26, 125015

[25] Uehara M, Uehara A, Kozawa K, et al. New antiperovskite superconductor $ZnNNi_3$, and related compounds $CdNNi_3$ and $InNNi_3$. Phys C Supercond Appl, 2010, 470, S688

[26] Shan L L, Feng S J, Liu X S, et al. Superconductivity and magnetic properties in antiperovskite nitride $ZnNNi_3$. Phys C Supercond Appl, 2022, 603, 1354158

[27] Shim J H, Kwon S K, Min B I. Electronic structures of antiperovskite superconductors $MgXNi_3$(X=B, C, and N). Phys Rev B, 2001, 64, 180510

[28] Zhang X H, Yin Y, Yuan Q, et al. Magnetoresistance reversal in antiperovskite compound $Mn_3Cu_{0.5}Zn_{0.5}N$. J Appl Phys, 2014, 115, 123905

[29] Sakakibara H, Ando H, Kuroki Y, et al. Magnetic properties and anisotropic magnetoresistance of antiperovskite nitride Mn_3GaN/Co_3FeN exchange-coupled bilayers. J Appl Phys, 2015, 117, 17D725

[30] Shibayama T, Takenaka K. Giant magnetostriction in antiperovskite Mn_3CuN. J Appl Phys, 2011, 109, 07A928

[31] Amraoui S, Feraoun A, Kerouad M. Theoretical study of the magnetic and magnetocaloric properties of the ZnFe3N antiperovskite. Curr Appl Phys, 2021, 31, 68

[32] Bilal M, Shafiq M, Khan B, et al. Antiperovskite compounds $SbNSr_3$ and $BiNSr_3$: Potential candidates for thermoelectric renewable energy generators. Phys Lett A, 2015, 379, 206

[33] Rani U, Kamlesh P K, Shukla A, et al. Emerging potential antiperovskite materials ANX_3 (A = P, As, Sb, Bi; X = Sr, Ca, Mg) for ther-

moelectric renewable energy generators. J Solid State Chem, 2021, 300, 122246
[34] Iikubo S, Kodama K, Takenaka K, et al. Magnetic structure and local lattice distortion in giant negative thermal expansion material $Mn_3Cu_{1-x}Ge_xN$. J Phys: Conf Ser, 2010, 251, 012014
[35] Hamada T, Takenaka K. Giant negative thermal expansion in antiperovskite Manganese nitrides. J Appl Phys, 2011, 109, 07E309
[36] Yu R, Weng H M, Fang Z, et al. Topological node-line semimetal and Dirac semimetal state in antiperovskite Cu_3PdN. Phys Rev Lett, 2015, 115, 036807
[37] Quintela C X, Campbell N, Shao D F, et al. Epitaxial thin films of Dirac semimetal antiperovskite Cu_3PdN. APL Mater, 2017, 5, 096103
[38] Goh W F, Pickett W E. Coemergence of Dirac and multi-weyl topological excitations in pnictide antiperovskites. Phys Rev B, 2018, 98, 125147
[39] Sreedevi P D, Vidya R, Ravindran P. Antiperovskite materials as promising candidates for efficient tandem photovoltaics: First-principles investigation. Mater Sci Semicond Process, 2022, 147, 106727
[40] Samanta D, Saha P K, Ghosh B, et al. Pressure-induced emergence of visible luminescence in lead free halide perovskite $Cs_3Bi_2Br_9$: Effect of structural distortion. J Phys Chem C, 2021, 125, 3432
[41] Cui Y Q, Cheng H, Tian H, et al. Pressure-induced reconstructive phase transitions, polarization with metallicity, and enhanced hardness in antiperovskite $MgCNi_3$. Phys Chem Chem Phys, 2021, 23, 18221
[42] Fu R J, Chen Y P, Yong X, et al. Pressure-induced structural transition and band gap evolution of double perovskite $Cs_2AgBiBr_6$ nanocrystals. Nanoscale, 2019, 11, 17004
[43] Wu L W, Dong Z Y, Zhang L, et al. High-pressure band-gap engineering and metallization in the perovskite derivative $Cs_3Sb_2I_9$. Chem Sus Chem, 2019, 12, 3971
[44] Cheng H, Mao A J, Yang S M, et al. Correction: Semiconductor-to-metal reconstructive phase transition and superconductivity of anti-perovskite Ca_3PN under hydrostatic pressure. J Mater Chem C, 2020, 8, 13090
[45] Samanta D, Chaudhary S P, Ghosh B, et al. Pressure-induced emission enhancement and bandgap narrowing: Experimental investigations and first-principles theoretical simulations on the model halide perovskite $Cs_3Sb_2Br_9$. Phys Rev B, 2022, 105, 104103
[46] Zhang L, Liu C M, Wang L R, et al. Pressure-induced emission enhancement, band-gap narrowing, and metallization of halide perovskite $Cs_3Bi_2I_9$. Angew Chem Int Ed, 2018, 57, 11213
[47] Li Q, Yin L X, Chen Z W, et al. High pressure structural and optical properties of two-dimensional hybrid halide perovskite $(CH_3NH_3)_3Bi_2Br_9$. Inorg Chem, 2019, 58, 1621
[48] Ma Z W, Liu Z, Lu S Y, et al. Pressure-induced emission of cesium lead halide perovskite nanocrystals. Nat Commun, 2018, 9, 1
[49] Szafrański M, Katrusiak A. Mechanism of pressure-induced phase transitions, amorphization, and absorption-edge shift in photovoltaic methylammonium lead iodide. J Phys Chem Lett, 2016, 7, 3458
[50] Momma K, Izumi F. *VESTA*: A three-dimensional visualization system for electronic and structural analysis. J Appl Cryst, 2008, 41, 653
[51] Wang X Y, Tian H, Li X, et al. Pressure effects on the structures and electronic properties of halide perovskite $CsPbX_3$ (X = I, Br, Cl). Phys Chem Chem Phys, 2021, 23, 3479
[52] Majumdar A, Adeleke A A, Chakraborty S, et al. Emerging piezochromism in lead free alkaline earth chalcogenide perovskite $AZrS_3$ (A = Mg, Ca, Sr and Ba) under pressure. J Mater Chem C, 2020, 8, 16392
[53] Tang G, Ghosez P, Hong J W. Band-edge orbital engineering of perovskite semiconductors for optoelectronic applications. J Phys Chem Lett, 2021, 12, 4227
[54] Ming W M, Shi H L, Du M H. Large dielectric constant, high acceptor density, and deep electron traps in perovskite solar cell material $CsGeI_3$. J Mater Chem A, 2016, 4, 13852
[55] Juarez-Perez E J, Sanchez R S, Badia L, et al. Photoinduced giant dielectric constant in lead halide perovskite solar cells. J Phys Chem Lett, 2014, 5, 2390
[56] Han D, Shi H L, Ming W M, et al. Unraveling luminescence mechanisms in zero-dimensional halide perovskites. J Mater Chem C, 2018, 6, 6398
[57] Takahashi A, Kumagai Y, Miyamoto J, et al. Machine learning models for predicting the dielectric constants of oxides based on high-throughput first-principles calculations. Phys Rev Materials, 2020, 4, 103801
[58] Zhao X Y, Vanderbilt D. Phonons and lattice dielectric properties of zirconia. Phys Rev B, 2002, 65, 075105
[59] Tang G, Xiao Z W, Hosono H, et al. Layered halide double perovskites $Cs_{3+n}M(II)_nSb_2X_{9+3n}$ (M = Sn, Ge) for photovoltaic applications. J Phys Chem Lett, 2018, 9, 43
[60] Zhao X G, Yang J H, Fu Y H, et al. Design of lead-free inorganic halide perovskites for solar cells via cation-transmutation. J Am Chem Soc, 2017, 139, 2630
[61] Shirayama M, Kadowaki H, Miyadera T, et al. Optical transitions in hybrid perovskite solar cells: Ellipsometry, density functional theory, and quantum efficiency analyses for $CH_3NH_3PbI_3$. Phys Rev Applied, 2016, 5, 014012
[62] Yokoyama T, Oba F, Seko A, et al. Theoretical photovoltaic conversion efficiencies of $ZnSnP_2$, $CdSnP_2$, and $Zn_{1-x}Cd_xSnP_2$ alloys. Appl Phys Express, 2013, 6, 061201
[63] Savory C N, Ganose A M, Travis W, et al. An assessment of silver copper sulfides for photovoltaic applications: Theoretical and experimental insights. J Mater Chem A, 2016, 4, 12648
[64] Han D, Du M H, Huang M L, et al. Ground-state structures, electronic structure, transport properties and optical properties of Ca-based anti-Ruddlesden-Popper phase oxide perovskites. Phys Rev Materials, 2022, 6, 114601
[65] Bush K A, Rolston N, Gold-Parker A, et al. Controlling thin-film stress and wrinkling during perovskite film formation. ACS Energy Lett, 2018, 3, 1225
[66] Guo L, Tang G, Hong J W. Mechanical properties of formamidinium halide perovskites $FABX_3$ (FA=$CH(NH_2)_2$; B=Pb, Sn; X=Br, I) by first-principles calculations. Chin Phys Lett, 2019, 36, 056201
[67] Tasnim A, Mahamudujjaman M, Asif Afzal M, et al. Pressure-dependent semiconductor–metal transition and elastic, electronic, optical, and thermophysical properties of orthorhombic SnS binary chalcogenide. Results Phys, 2023, 45, 106236
[68] Rong Z, Zhi C, Jun C. *Ab initio* calculation of mechanical, electronic and optical characteristics of chalcogenide perovskite $BaZrS_3$ at high pressures. Acta Crystallogr C, 2022, 78, 570
[69] Wu Z J, Zhao E J, Xiang H P, et al. Publisher's Note: Crystal structures and elastic properties of superhard IrN_2 andIrN_3 from first principles. Phys Rev B, 2007, 76, 059904
[70] Hill R. The elastic behaviour of a crystalline aggregate. Proc Phys Soc A, 1952, 65, 349
[71] Hadi M A, Nasir M T, Roknuzzaman M, et al. First-principles prediction of mechanical and bonding characteristics of new T_2 superconductor Ta_5GeB_2. Phys Status Solidi B, 2016, 253, 2020
[72] Li S, Zhao S G, Chu H Q, et al. Unraveling the factors affecting the mechanical properties of halide perovskites from first-principles calculations. J Phys Chem C, 2022, 126, 4715
[73] Li Z G, Qin Y, Dong L Y, et al. Elastic and electronic origins of strain stabilized photovoltaic γ-$CsPbI_3$. Phys Chem Chem Phys, 2020, 22, 12706
[74] Elahmar M H, Rached H, Rached D, et al. Structural, mechanical, electronic and magnetic properties of a new series of quaternary Heusler alloys CoFeMnZ (Z=Si, As, Sb): A first-principle study. J

Magn Magn Mater, 2015, 393, 165
[75] Saravana Karthikeyan S K S, Santhoshkumar P, Joe Y C, et al. Understanding of the elastic constants, energetics, and bonding in dicalcium silicate using first-principles calculations. J Phys Chem C, 2018, 122, 24235

Chunbao Feng got his doctor's degree in 2013 from University of Electronic Science and Technology of China and his master's degree in 2008 from Shanghai University. Now he is an associated professor at School of Science, Chongqing University of Posts and Telecommunications. His research focuses on the material design in the perovskite-based solar cell absorbers.

Gang Tang received his PhD from Beijing Institute of Technology in 2019. Then, he did postdoctoral studies at University of Liège in Belgium. Currently, he is an Associate professor at Advanced Research Institute of Multidisciplinary Science, Beijing Institute of Technology. His research focuses on the first-principles simulations of optoelectronic semiconductors.